

See discussions, stats, and author profiles for this publication at: <https://www.researchgate.net/publication/330513080>

# Active Disturbance Rejection Control of a Flying-Wing Tailsitter in Hover Flight

Conference Paper · October 2018

DOI: 10.1109/ROS.2018.8594470

CITATIONS

5

READS

1,238

4 authors, including:



Yunjie Yang

Tsinghua University

8 PUBLICATIONS 17 CITATIONS

[SEE PROFILE](#)



Jihong Zhu

Tsinghua University

27 PUBLICATIONS 52 CITATIONS

[SEE PROFILE](#)

Some of the authors of this publication are also working on these related projects:



Tailsitter UAV [View project](#)

# Active Disturbance Rejection Control of a Flying-Wing Tailsitter in Hover Flight\*

Yunjie Yang<sup>1</sup>, Jihong Zhu<sup>1</sup>, Xiaojun Zhang<sup>2</sup> and Xiangyang Wang<sup>1</sup>

**Abstract**—This paper presents the development and hovering control of a tailsitter unmanned aerial vehicle (UAV) that merges long endurance and vertical takeoff and landing (VTOL) abilities. The designed tailsitter contains one flying-wing with two motors and two elevons. Vehicle aerodynamics and a six-degrees-of-freedom (6-DOF) model are especially developed for the tailsitter. To achieve a good performance in outdoor stationary hovering and accurate vertical flying, the active disturbance rejection control (ADRC) for attitude controller is proposed. With signals from extended state observer (ESO) and tracking differentiator (TD), ADRC decouples the system model into a controllable chain of integrators. Based on the decoupled system dynamics, the motion of tailsitter can be easily handled by developed position controller. Experimental results are presented to corroborate the effectiveness of the controller in disturbance rejection.

## I. INTRODUCTION

Unmanned aerial vehicles (UAVs) are used in a variety of applications, ranging from agricultural seeding and express delivery, to dangerous rescue and military action [1]. Generally, UAVs are divided into two categories. One is the fixed-wing aircrafts with long endurance and cruise speed, but they usually need runways to take off and land. The other one is the rotary-wing aircrafts which can vertically take off and land, but lacks of the endurance or cruise speed [2]. To integrate the advantages of both aircrafts, one of the better choices is the tailsitter aircraft [3,4,5], which switches between horizontal and vertical modes by changing the fuselage pitch angle of  $90^\circ$ .

As shown in Fig. 1, we designed and manufactured a dual-rotor tailsitter UAV based on a kind of fixed-wing aircraft. The UAV can achieve VTOL abilities without adding other mechanical complexity. Different from long distance flights in the horizontal mode, the outdoor stationary hovering and accurate vertical flying mainly contribute to precise adjustments of the UAV attitude and position. But the maneuvers are difficult to control due to unknown nonlinearity and uncertain coupling in the system dynamics [6-11]. A model reference adaptive quaternion backstepping control method was derived in [6]. The authors use a data-weighting recursive least-squares algorithm for the online identification of system parameters. A nonlinear feedback



Fig. 1. The designed tailsitter hovering in the air. (Video available at <https://youtu.be/2jecZo81iGc>)

control law based on the Lyapunov approach was proposed in [7] for VTOL UAVs to stabilize reference trajectories of thrust, velocity and position. However, the assumption that the forces acting on the vehicle are free with attitudes is not applicable to our tailsitter. In [8], the hover dynamics were divided into longitudinal and lateral directions, and the heading was included in the latter one. Both directions were controlled by the LQR controller, which generated linear models and LQR gains based on current vehicle state every  $200ms$ . A model based wind estimation, which only used an IMU, a GPS and a magnetometer, for a hovering VTOL tailsitter was presented in [9] to achieve robust outdoor flight. But it can only estimate very slow-changing wind in real flight tests. Overall, most of these control approaches are model based, which brings difficulties in the engineering application. Although the PID controller [11] is independent of system model, its performance in disturbance rejection is hard to guarantee.

In our previous work [5], a PID-based attitude controller has been developed for a thrust-vectorized tailsitter. In this paper, to achieve a better performance in the hovering and vertical flying, a synthesized control strategy is proposed for the new flying-wing tailsitter. The position controller handles the motion of tailsitter by converting command body velocities into desired Euler angles. With active disturbance rejection control (ADRC) developed for the attitude controller, an extended state observer (ESO) is designed to estimate unknown dynamics and uncertain disturbances. The signals from ESO and tracking differentiator (TD) decouple the system model into a controllable chain of integrators by nonlinear state error feedback (NLSEF). Experiments in our tailsitter demonstrate excellent performance of the controller

\*Research supported by National Natural Science Foundation of China (Grant Nos. 61603210 and 61673240).

<sup>1</sup>Yunjie Yang, Jihong Zhu and Xiangyang Wang are with the Beijing National Research Center for Information Science and Technology (BNRist), Department of Computer Science and Technology, Tsinghua University, Beijing 100084, China, [yyj15@mails.tsinghua.edu.cn](mailto:yyj15@mails.tsinghua.edu.cn)

<sup>2</sup>Xiaojun Zhang is with the Department of Automation, Tsinghua University, Beijing 100084, China

in disturbance rejection.

The remainder of this paper is organized as follows: the system configuration of our tailsitter is presented in section II. The nonlinear dynamic model is derived in section III, followed by the position and attitude control strategy in section IV. Experimental results are shown in section V. Conclusions and future works are given in section VI.

## II. SYSTEM CONFIGURATION

This section presents the tailsitter we designed and manufactured in more details, including aircraft design in subsection II-A, coordinate systems in II-B and actuation principle in II-C.

### A. Aircraft Design

Fig. 2 shows the mechanical structure of the designed flying-wing tailsitter. All parts of the vehicle are newly developed. To balance the strength and the weight of the tailsitter, the fuselage is made by aviation laminates and carbon plates. The vehicle skeleton is covered with heat shrinkable skin. Two CW/CCW carbon propellers with the diameter of 16" driven by 600W brushless electrical motors are chosen as the system propulsion. Two 6s LIPO batteries are used to supply power.

The airframe consists of one flying-wing with two elevons. The profile of the wing is the MH91 whose wing area is  $0.478m^2$ , span is  $1.2m$  and chord length is  $0.438m$ . The Pixhawk 2.1 autopilot [12] is adopted as the core avionics. The all-up-weight of the tailsitter is  $2.23kg$ .

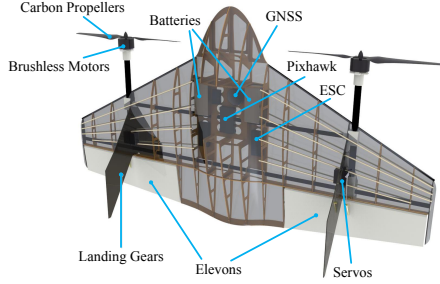


Fig. 2. Hardware configuration of the tailsitter

### B. Coordinate Systems

As Fig. 3 shows, the North-East-Down (NED) coordinate system is chosen as the earth frame, where  $x_e$  is north,  $y_e$  is east and  $z_e$  is down. Since we mainly focus on the hovering and vertical flying of the vehicle, vertical body frame is adopted to avoid singularity in the controller design: the original point coincides with the center of gravity (C.G.),  $x_b$  points to the belly of the vehicle,  $z_b$  points to the tail of the vehicle and  $y_b$  is determined by the right-hand principle.  $x_b$  parallels to  $x_e$  when the vehicle vertically faces the north.

### C. Actuation Principle

The tailsitter uses a minimum combination of motors and elevons to control its attitude during the whole flight envelope. As shown in Fig. 4(a), differential thrust of two propellers is used to control the axis  $x_b$  of the vehicle. The

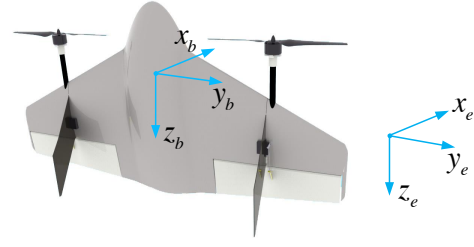


Fig. 3. Earth and body coordinate systems

vehicle axis  $y_b$  is controlled by equal elevons deflections (Fig. 4(b)) and the axis  $z_b$  is similarly steered by differential elevons deflections (Fig. 4(c)). The elevons have a range of  $\pm 30^\circ$ , and the down deflection is defined as positive. The moments of pitch and yaw are determined by both propeller slipstream and air flow diverted by the elevons.

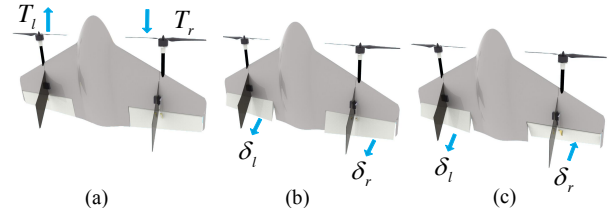


Fig. 4. Actuation principle of the tailsitter

## III. MODELING

The aerodynamics and six-degrees-of-freedom (6-DOF) equations of motion for the tailsitter are derived in this section. The vehicle is considered to be rigid and the earth frame is regarded as an inertial reference. The vehicle dynamics are described by its position, orientation, velocity and angular velocity.

### A. Vehicle Aerodynamics

For our tailsitter, the main wing almost lies in the near-field region, thus the propeller slipstream velocity can be derived by the momentum theory and the continuity equation [13], which is expressed as

$$u_0 = \sqrt{\frac{2T}{\rho A} + v_\infty^2} \left[ 1 + \frac{l_p/R}{\sqrt{1 + (l_p/R)^2}} \right] \quad (1)$$

where  $T$  is the propeller thrust,  $\rho$  is the air density,  $A$  is the propeller disk area,  $v_\infty$  is the velocity of freestream,  $l_p$  is the distance between center of elevons and propeller disk,  $R$  is the radius of the propeller. Then the airspeed which shows the flow conditions of the airframe can be calculated as

$$\mathbf{V} = \mathbf{V}_{prop} + \mathbf{V}_{wind} + \mathbf{V}_{body} \quad (2)$$

where  $\mathbf{V}_{prop} = [0, 0, u_0]$ , which is the major term in vertical flying.  $\mathbf{V}_{wind}$  is the wind speed and  $\mathbf{V}_{body}$  is the ground speed projected to the body frame. The angle of attack  $\alpha$  and sideslip angle  $\beta$  are defined as

$$\alpha = \arctan\left(-\frac{v_x}{v_z}\right), \quad \beta = \arcsin\left(\frac{v_y}{\|\mathbf{V}\|}\right) \quad (3)$$

where  $v_x$ ,  $v_y$  and  $v_z$  are three components of  $\mathbf{V}$ . Therefore, the aerodynamic forces produced by the wing and elevons can be calculated as

$$\begin{aligned} L &= [C_{L0}(\alpha, \beta) + C_{L\delta}(\alpha, \delta_l) + C_{L\delta}(\alpha, \delta_r)] \bar{q}S \\ D &= [C_{D0}(\alpha, V) + C_{D\delta}(\alpha, \delta_l) + C_{D\delta}(\alpha, \delta_r)] \bar{q}S \quad (4) \\ F_{Ay} &= [C_{Y0}(\alpha, \beta) - C_{Y\delta}(\alpha, \delta_l) + C_{Y\delta}(\alpha, \delta_r)] \bar{q}S \end{aligned}$$

where  $L$ ,  $D$  and  $F_{Ay}$  are the lift, drag and side forces respectively.  $\delta_l$  and  $\delta_r$  represent the deflection angles of the left elevon and right elevon.  $\bar{q} = \frac{1}{2}\rho\|\mathbf{V}\|^2$  is the dynamic pressure.  $S$  is the wing area. Since (4) is calculated at stability axes, the aerodynamic forces along body axes are

$$\begin{pmatrix} \bar{X} \\ \bar{Y} \\ \bar{Z} \end{pmatrix} = \begin{pmatrix} -(D \sin \alpha + L \cos \alpha) \\ F_{Ay} \\ D \cos \alpha - L \sin \alpha \end{pmatrix} \quad (5)$$

The aerodynamic moments along body axes are similarly expressed as

$$\begin{aligned} \bar{L} &= [C_{\bar{L}0}(\alpha, \beta) - C_{\bar{L}\delta}(\alpha, \delta_l) + C_{\bar{L}\delta}(\alpha, \delta_r)] \bar{q}Sb \\ \bar{M} &= [C_{\bar{M}0}(\alpha, \beta) + C_{\bar{M}\delta}(\alpha, \delta_l) + C_{\bar{M}\delta}(\alpha, \delta_r)] \bar{q}S\bar{c} \quad (6) \\ \bar{N} &= [C_{\bar{N}0}(\alpha, \beta) - C_{\bar{N}\delta}(\alpha, \delta_l) + C_{\bar{N}\delta}(\alpha, \delta_r)] \bar{q}Sb \end{aligned}$$

where  $\bar{L}$ ,  $\bar{M}$  and  $\bar{N}$  are the rolling, pitching and yawing moments respectively.  $b$  is the wing span and  $\bar{c}$  is the chord length.

The aerodynamic coefficients of (4) and (6) are derived by the Vortex Lattice Method [14] with XFLR5 [15] as an analysis tool. About 120 sets of VLM data are calculated based on factors like the angle of attack, the sideslip angle, the airspeed, the elevons deflection angles and so on. In order to generate a comprehensive database, all coefficients are fitted into 2-order or 3-order polynomials about two major factors. The  $C_{*0}$  terms are contributed by the main wing and the  $C_{*\delta}$  terms are contributed by the elevons.

Fig. 5 shows  $C_{\bar{M}\delta}$  and  $C_{\bar{N}\delta}$  for examples, which will be used in control allocation in section IV-C. The range of the angle of attack at vertical mode is about  $-15^\circ \sim 15^\circ$ , which is estimated according to (3) with conclusions in [13] as the theoretical support. Other coefficients are omitted due to space limitations.

## B. 6-DOF Equations of Motion

Forces acting on the vehicle consist of propeller thrust, gravity and aerodynamic forces. For our tailsitter, the resultant thrust of left propeller and right propeller coincides with the negative  $z_b$  axis but it does not pass through the center of gravity. The complete body-frame force equation is formed as

$$\begin{aligned} m(\dot{u} + qw - rv) &= \bar{X} - mg \sin \theta \\ m(\dot{v} + ru - pw) &= \bar{Y} + mg \cos \theta \sin \phi \\ m(\dot{w} + pv - qu) &= \bar{Z} + mg \cos \theta \cos \phi - (T_l + T_r) \end{aligned} \quad (7)$$

where  $T_l$  and  $T_r$  represent the thrust generated by the left and right propeller.  $u$ ,  $v$  and  $w$  are velocities while  $p$ ,  $q$  and  $r$  are the angular velocities along body axes.  $\phi$ ,  $\theta$  and  $\psi$  are

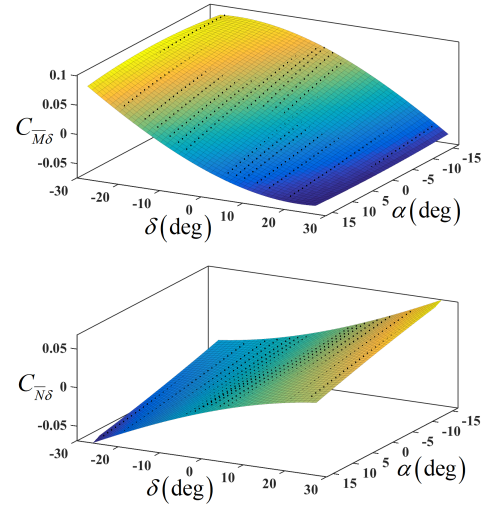


Fig. 5. Examples of coefficients with VLM

the roll, pitch and yaw angle of the tailsitter respectively.  $m$  is the mass of vehicle and  $g$  is the gravitational acceleration. The complete body-frame moment equation is formed as

$$\begin{aligned} \dot{p}I_x + qr(I_z - I_y) - (\dot{r} + pq)I_{xz} &= \bar{L} + (T_r - T_l)l_y \\ \dot{q}I_y + pr(I_x - I_z) - (r^2 - p^2)I_{xz} &= \bar{M} + (T_l + T_r)l_x \quad (8) \\ \dot{r}I_z + pq(I_y - I_x) - (\dot{p} - qr)I_{xz} &= \bar{N} + (M_l + M_r) \end{aligned}$$

where  $l_y$  denotes the distance between propeller thrust axis and the center of gravity along  $y_b$ .  $l_x$  denotes the distance between resultant thrust axis and the center of gravity along  $x_b$ .  $M_l$  and  $M_r$  are the moments generated due to the rotation of motors and propellers.  $I_x$ ,  $I_y$ ,  $I_z$  and  $I_{xz}$  are the moments of inertia. For our tailsitter,  $I_x = 0.16017 \text{ kgm}^2$ ,  $I_y = 0.04085 \text{ kgm}^2$ ,  $I_z = 0.19866 \text{ kgm}^2$  and  $I_{xz} = 0.00008 \text{ kgm}^2$ .

The rotation part of vehicle kinematics describes the relation between Euler angles and angular velocities, which are

$$\begin{aligned} \dot{\phi} &= p + \tan \theta (q \sin \phi + r \cos \phi) \\ \dot{\theta} &= q \cos \phi - r \sin \phi \\ \dot{\psi} &= \frac{q \sin \phi + r \cos \phi}{\cos \theta} \end{aligned} \quad (9)$$

The translation part describes the displacement of the UAV center of gravity with respect to velocity, which are

$$\begin{bmatrix} \dot{x}_E \\ \dot{y}_E \\ \dot{z}_E \end{bmatrix} = \begin{bmatrix} c_\psi c_\theta & c_\psi s_\theta s_\phi - s_\psi c_\phi & c_\psi s_\theta c_\phi + s_\psi s_\phi \\ s_\psi c_\theta & s_\psi s_\theta s_\phi + c_\psi c_\phi & s_\psi s_\theta c_\phi - c_\psi s_\phi \\ -s_\theta & c_\theta s_\phi & c_\theta c_\phi \end{bmatrix} \begin{bmatrix} u \\ v \\ w \end{bmatrix} \quad (10)$$

where  $s_\theta = \sin \theta$ ,  $c_\theta = \cos \theta$ , the transfer matrix is called as the directional cosine matrix.  $x_E$ ,  $y_E$  and  $z_E$  are the positions expressed in the earth frame.

## IV. CONTROL SYSTEM

In this section, the position and attitude controllers are developed for the tailsitter, whose structure is shown in Fig. 6. The active disturbance rejection control for attitude controller can decouple system by estimating unknown dynamics and uncertain disturbance, which simplifies the design of position controller.

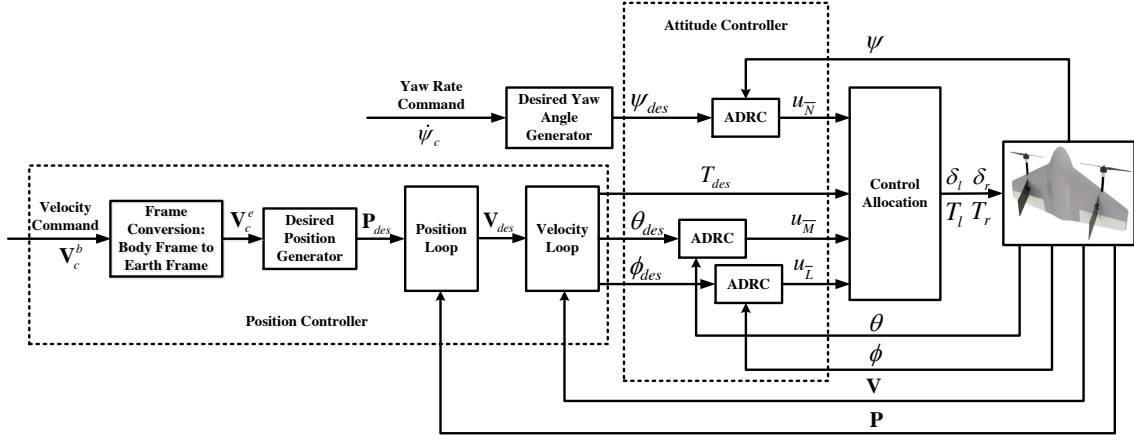


Fig. 6. The structure of proposed controller

### A. Position Controller

The position controller takes the motion control of tailsitter in three-dimensional space. Its input is the velocity command along the three body axes, and the output is desired pitch angle, roll angle and propeller thrust. The desired yaw angle  $\psi_{des}$  is obtained by the integral of the input yaw rate separately. There are two loops in the position controller: the outer one is a position loop and the inner one is a velocity loop.

Firstly, the command body velocity  $\mathbf{V}_c^b$  is projected onto the three earth axes by rotating the yaw angle of the vehicle:

$$\mathbf{V}_c^e = R_\psi \mathbf{V}_c^b = \begin{bmatrix} \cos \psi & -\sin \psi & 0 \\ \sin \psi & \cos \psi & 0 \\ 0 & 0 & 1 \end{bmatrix} \mathbf{V}_c^b \quad (11)$$

Then it is integrated to get the desired 3-dimensional location in the earth frame:

$$\mathbf{P}_{des}(k) = \mathbf{P}_{des}(k-1) + \mathbf{V}_c^e(k-1) \cdot T_s \quad (12)$$

where  $T_s$  is the sampling time. With the estimated vehicle location  $\mathbf{P}(k)$ , a proportional controller is used in the position loop to get desired velocity:

$$\mathbf{V}_{des}(k) = \mathbf{K}_{p-pos} \cdot [\mathbf{P}_{des}(k) - \mathbf{P}(k)] \quad (13)$$

where  $\mathbf{K}_{p-pos}$  is a positive definite gain matrix.

PI controller with gravity feedforward is used for the velocity loop, which computes the desired force vector with the estimated vehicle velocity  $\mathbf{V}(k)$ :

$$\mathbf{F}_{des} = \mathbf{K}_{p-vel} \cdot \mathbf{e} + \mathbf{K}_{i-vel} \cdot \int \mathbf{e} dt + m\mathbf{g} \quad (14)$$

where  $\mathbf{e} = \mathbf{V}_{des}(k) - \mathbf{V}(k)$  is the velocity error.  $\mathbf{K}_{p-vel}$  and  $\mathbf{K}_{i-vel}$  are positive definite gain matrices.  $\mathbf{g} = [0, 0, g]$  represents the gravity of the vehicle.

Based on (14), the desired thrust can be obtained by projecting  $\mathbf{F}_{des}$  onto the  $z$  axis in the body frame:

$$T_{des} = \mathbf{F}_{des} \cdot \mathbf{z}_b \quad (15)$$

where  $\mathbf{z}_b$  is the projection vector of body  $z$  axis at the earth frame. The desired pitch angle and roll angle can be calculated as:

$$\theta_{des} = \arctan \left[ \frac{\hat{\mathbf{F}}_{des}(1) \cdot \cos \psi_{des} + \hat{\mathbf{F}}_{des}(2) \cdot \sin \psi_{des}}{\hat{\mathbf{F}}_{des}(3)} \right] \quad (16)$$

$$\phi_{des} = -\text{sgn}(\hat{\mathbf{F}}_{des}(2)) \cdot \arccos \left[ \frac{\hat{\mathbf{F}}_{des}(3)}{\cos \theta_{des}} \right] \quad (17)$$

where  $\hat{\mathbf{F}}_{des} = \mathbf{F}_{des} / \|\mathbf{F}_{des}\|$ ,  $\text{sgn}(\bullet)$  is the sign function.

### B. Attitude Controller

In this subsection, active disturbance rejection control (ADRC) law is developed for the roll, pitch and yaw control of our tailsitter. As shown in Fig. 6, the inputs of ADRC are desired euler angles, and the outputs are desired moments to obtain the desired inputs. Since the establishments of ADRC in the pitch and yaw channels are similar to the roll channel, we will just derive the roll-ADRC.

Because the vertical flying of the tailsitter mainly works for the precise adjustment of the vehicle position, the euler angles are small. The roll angle rate can be simplified as

$$\dot{\phi} = p \quad (18)$$

And we rewrite the roll axis in (8) as follows

$$\begin{aligned} \dot{p} &= \frac{1}{I_x} [\bar{L} + (T_r - T_l) l_y] + \frac{I_{xz}}{I_x} (\dot{r} + pq) + \frac{I_y - I_z}{I_x} qr \\ &= \frac{1}{I_x} [\bar{L} + (\dot{r} + pq) I_{xz}] + \frac{1}{I_x} (T_r - T_l) l_y + \frac{I_y - I_z}{I_x} qr \\ &= F_x(\phi, p, \dots) + b_x u_L + \frac{I_y - I_z}{I_x} qr \end{aligned} \quad (19)$$

where  $b_x = 1/I_x$  is a known quantity.  $u_L = (T_r - T_l) l_y$  is the roll control moment, which is produced by differential thrust of two propellers.  $F_x = [\bar{L} + (\dot{r} + pq) I_{xz}] / I_x$  is the sum of unknown dynamics and uncertain disturbance, its estimation is the key step of ADRC.



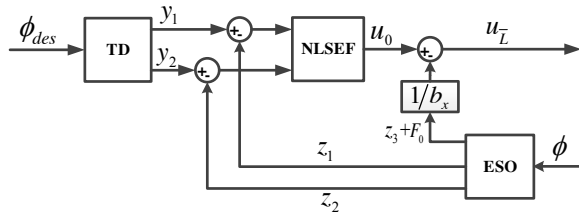


Fig. 7. The structure of ADRC

The structure of roll-ADRC is shown in Fig. 7, we will develop it in the following three steps.

**Step1: Extended State Observer (ESO)**

Take  $x_1 = \phi$  and  $x_2 = p$ , the roll dynamics can be written as

$$\begin{aligned}\dot{x}_1 &= x_2 \\ \dot{x}_2 &= F_x(x_1, x_2, \delta(t)) + b_x u_L + F_0\end{aligned}\quad (20)$$

where  $\delta(t)$  describes the uncertain factors in  $F_x$ ,  $F_0 = (I_y - I_z)/I_x \cdot q r$  can be easily get from ESO in the pitch and yaw channels. By adding a new state variable  $x_3 = F_x(x_1, x_2, \delta(t))$  and assuming  $\dot{x}_3 = G_x(x_1, x_2, \delta(t))$ , (20) extends into

$$\begin{aligned}\dot{x}_1 &= x_2 \\ \dot{x}_2 &= x_3 + b_x u_L + F_0 \\ \dot{x}_3 &= G_x(x_1, x_2, \delta(t))\end{aligned}\quad (21)$$

To establish ESO, we firstly define a piecewise error function as follows

$$fal(e, \alpha, \varepsilon) = \begin{cases} |e|^\alpha sgn(e) & |e| > \varepsilon \\ e/\varepsilon^{1-\alpha} & |e| \leq \varepsilon \end{cases}\quad (22)$$

where  $e$  is the error to map,  $\alpha \in (0, 1]$  is a parameter to reflect its change rate. When the observe error is larger than the maximum linear zone  $\varepsilon$ , a variable-gain nonlinear error mapping is used to obtain a fast convergence. Otherwise a linear error mapping is used to avoid oscillations in the nonlinear mapping. This feature ensures a more reasonable application of observe errors in ESO. Take variables  $z_1$ ,  $z_2$  and  $z_3$  as three states to observe  $x_1$ ,  $x_2$  and  $x_3$  respectively, the ESO of (21) is given bases on (22):

$$\begin{aligned}\dot{z}_1 &= z_2 - \beta_1 e \\ \dot{z}_2 &= z_3 - \beta_2 \cdot fal(e, \alpha_1, \varepsilon) + b_x u_L + F_0 \\ \dot{z}_3 &= -\beta_3 \cdot fal(e, \alpha_2, \varepsilon)\end{aligned}\quad (23)$$

where  $e = z_1 - x_1$  is the observe error,  $\beta_1$ ,  $\beta_2$  and  $\beta_3$  are adjustable parameters to achieve control objectives. ESO is similar to full-order state observers of linear systems. Following the approach in [16], it can be proved that if  $|G_x(x_1, x_2, \delta(t))| < \sigma_0$ , the observe errors satisfy with

$$\begin{aligned}\lim_{t \rightarrow \infty} |z_1(t) - x_1(t)| &< \left(\frac{\sigma_0}{\beta_3}\right)^{1/\alpha_2} \\ \lim_{t \rightarrow \infty} |z_2(t) - x_2(t)| &< \beta_1 \left(\frac{\sigma_0}{\beta_3}\right)^{1/\alpha_2} \\ \lim_{t \rightarrow \infty} |z_3(t) - x_3(t)| &< \beta_2 \left(\frac{\sigma_0}{\beta_3}\right)^{1/\alpha_2}\end{aligned}\quad (24)$$

Therefore, the observer state  $z_3$  can approximate  $x_3 = F_x(x_1, x_2, \delta(t))$  within a certain error range. In the following steps,  $z_3$  will be fed back to control input to compensate

unknown disturbances. For the convenience of code realization, the discrete form of ESO is listed as follows.

$$\begin{aligned}e(k) &= z_1(k) - x_1(k) \\ z_1(k+1) &= z_1(k) + (z_2(k) - \beta_1 e(k)) \tilde{T}_s \\ z_2(k+1) &= z_2(k) + (z_3(k) - \beta_2 fal + b_x u_L + F_0) \tilde{T}_s \\ z_3(k+1) &= z_3(k) - \beta_3 fal \cdot \tilde{T}_s\end{aligned}\quad (25)$$

where  $\tilde{T}_s$  is sampling time of ADRC law, which is smaller than the sampling time of position controller in general.

For the pitch and yaw channels, ESOs reflect their unknown dynamics and external disturbances respectively, including the counter-moment due to rotation of propellers, undesired pitch moment due to the displacement between resultant thrust axis and center of gravity and so on. This is the major difference in the realization of three ADRC controllers.

**Step2: Tracking Differentiator (TD)**

The differential of classic PID control amplifies noises significantly. Thus the signal is distorted and cannot be used directly. To solve the problem, TD is proposed in this section to track command signals and obtain a noise-free differential. Consider the dual integrator series system

$$\begin{aligned}\dot{y}_1 &= y_2 \\ \dot{y}_2 &= u, |u| \leq u_m\end{aligned}\quad (26)$$

where  $u_m$  is the magnitude of control input. To make  $y_1(t)$  tracks the desired roll angle  $\phi_{des}(t)$  within a minimum time, we adopt the time-optimal control [17], which is

$$u(t) = -u_m \cdot sgn\left(y_1 - \phi_{des}(t) + \frac{y_2 |y_2|}{2u_m}\right)\quad (27)$$

Under the control input (27),  $y_1(t)$  will track  $\phi_{des}(t)$  closely enough in the shortest time. Therefore, the state variable  $y_2(t)$  can be regarded as an approximate differential of the command signal  $\phi_{des}(t)$ . However, for discrete form of (26):

$$\begin{aligned}y_1(k+1) &= y_1(k) + \tilde{T}_s \cdot y_2(k) \\ y_2(k+1) &= y_2(k) + \tilde{T}_s \cdot u(k)\end{aligned}\quad (28)$$

Its discrete system state is hard to accurately stay on the optimal switching trajectory under the control input (27), which will lead to high frequency oscillations. Therefore, we extend the optimal switching trajectory in (27) to a suboptimal switching zone:

$$g = \begin{cases} y_2 - sgn(\lambda) \frac{u_m}{2} \left( \tau - \sqrt{8|\lambda|/u_m + \tau^2} \right) & |\lambda| \geq \eta_0 \\ y_2 + \lambda/\tau & |\lambda| < \eta_0 \end{cases}\quad (29)$$

where  $\tau = n\tilde{T}_s$ ,  $\eta = \tau u_m$  and  $\eta_0 = \eta\tau$ .  $\lambda = y_1 - \phi_{des} + \tau y_2$  reflects the signal we need to track. The control input of system (26) is given as

$$u(k) = -u_m \cdot \begin{cases} sgn(g) & |g| > \eta \\ g/\eta & |g| \leq \eta \end{cases}\quad (30)$$

Under the input (30),  $y_1(k)$  is a close approximation of  $\phi_{des}(k)$ , and  $y_2(k)$  is a good-quality differential of  $\phi_{des}(k)$ .

## V. EXPERIMENTAL VERIFICATION

### Step3: Nonlinear State Error Feedback (NLSEF)

With the command signals from TD and the feedback signals from ESO, the state error is defined as

$$\begin{aligned} e_1 &= y_1 - z_1 \\ e_2 &= y_2 - z_2 \end{aligned} \quad (31)$$

Applying the error function (22) again, we firstly define

$$u_0 = k_1 \cdot \text{fal}(e_1, \tilde{\alpha}_1, \varepsilon) + k_2 \cdot \text{fal}(e_2, \tilde{\alpha}_2, \varepsilon) \quad (32)$$

Note that the state variable  $z_3$  of ESO is the estimation of unknown disturbances  $F_x(x_1, x_2, \delta(t))$ . Therefore, with control input

$$u_{\bar{L}} = u_0 - \frac{1}{b_x}(z_3 + F_0) \quad (33)$$

System (20) turns into

$$\begin{aligned} \dot{x}_1 &= x_2 \\ \dot{x}_2 &= b_x u_0 \end{aligned} \quad (34)$$

which is a controllable chain of integrators.

The stability of ADRC is easy to prove because of independence among the ESO, TD and NLSEF. First, the phase plane method used in the derivation of the TD ensures a zero-error and noise-free recurrence of command signals. While from (24), the unknown dynamics and uncertain disturbances of the system are accurately observed by the ESO. Based on these high-quality signals, the NLSEF of system (20) equivalents to nonlinear PD control of dual integrator system. The stability and effectiveness is easy to derive following the analysis in [18] and thus omitted here. As shown in section V, several experiments illustrate that command signals are well tracked.

### C. Control Allocation

The ADRC controllers for the pitch and yaw channels can be derived similarly as the roll channel. The relationships between the control moments and elevons deflection angles are

$$\begin{aligned} u_{\bar{M}} &= \frac{\partial C_{\bar{M}\delta}}{\partial \delta} q S \bar{c} \cdot (\delta_l + \delta_r) \\ u_{\bar{N}} &= \frac{\partial C_{\bar{N}\delta}}{\partial \delta} q S b \cdot (-\delta_l + \delta_r) \end{aligned} \quad (35)$$

where  $u_{\bar{M}}$  is the pitch control moment, which is produced by equal elevons deflections. And  $u_{\bar{N}}$  is the yaw control moment, which is produced by differential elevons deflections.  $C_{\bar{M}\delta}$  and  $C_{\bar{N}\delta}$ , which are the only two coefficients will be used in actual flights, are given in the Fig. 5. From (35), we can get

$$\begin{bmatrix} \delta_l \\ \delta_r \end{bmatrix} = \frac{1}{2} \begin{bmatrix} 1 & -1 \\ 1 & 1 \end{bmatrix} \begin{bmatrix} \frac{u_{\bar{M}}}{\partial C_{\bar{M}\delta} / \partial \delta \cdot q S \bar{c}} \\ \frac{u_{\bar{N}}}{\partial C_{\bar{N}\delta} / \partial \delta \cdot q S b} \end{bmatrix} \quad (36)$$

The thrust of two propellers can be determined by the desired thrust and roll control moment, which is

$$\begin{bmatrix} T_l \\ T_r \end{bmatrix} = \frac{1}{2} \begin{bmatrix} 1 & -1 \\ 1 & 1 \end{bmatrix} \begin{bmatrix} T_{des} \\ u_{\bar{L}}/l_y \end{bmatrix} \quad (37)$$

This section presents the outdoor hovering and vertical flying results of our tailsitter. The experiments are conducted at a windy day to demonstrate the disturbance rejection ability of the controller. The wind blows from north to south at the speed of  $3 \sim 4 \text{ m/s}$ , which is measured by a handheld anemometer in ground. Experiments with the proposed ADRC and standard PID, which is used in the PX4 open source project [12], are conducted to make a comparison for the attitude control of the tailsitter.

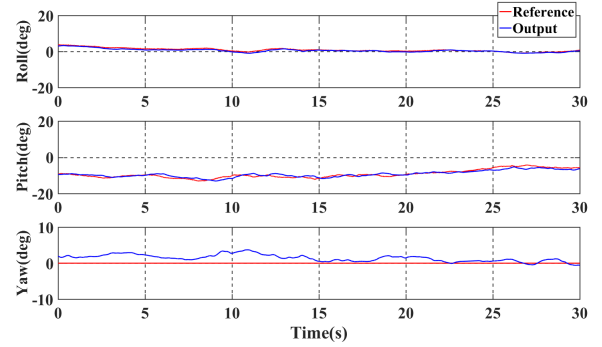


Fig. 8. Attitude of the tailsitter with ADRC in hovering

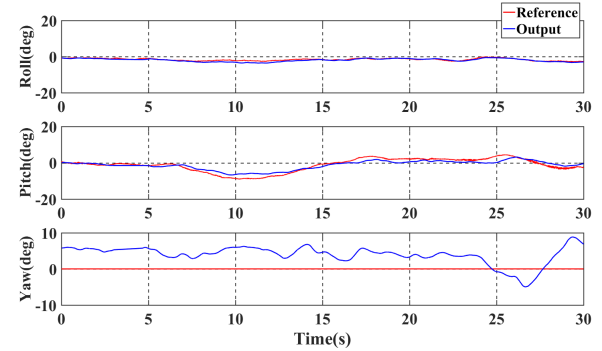


Fig. 9. Attitude of the tailsitter with PID in hovering

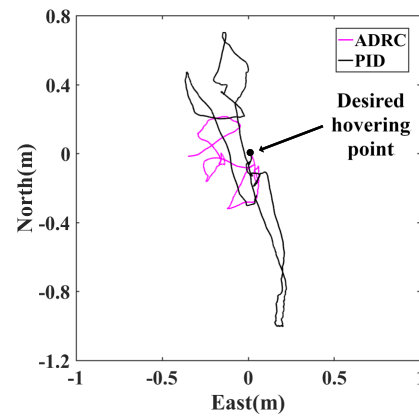


Fig. 10. Top down view of the position in hovering

In the first test, the tailsitter is commanded to hold still for about 30 seconds with its belly facing the wind. There is no manual control during the hovering. Fig. 8 and 9 illustrate the attitude of the hovering UAV under the ADRC and PID controller respectively. It can be seen from Fig. 8 that the tailsitter tilts a negative pitch angle with the ADRC. Thus a horizontal propeller thrust component is produced to resist

the wind. But the PID controller barely compensates the disturbances. The top down view of the vehicle position during hovering also confirms this point: as can be seen from Fig. 10, the error between the desired and actual hovering position in north-south direction with the PID controller (about 1.7080m) is about three times as the error with the ADRC (about 0.5346m). The heading of the UAV with the ADRC is also more stable than that with the PID.

In the second test, the tailsitter is commanded to fly 15 meters forward and then back with its belly facing the wind, which is the harshest situation. Fig. 11 and 12 illustrate the attitude of the flying UAV under the ADRC and PID controller respectively. It can be seen that the pitch angle holds a high quality tracking in reference commands with the ADRC, while oscillations occur during the forward flying with the PID controller. Meanwhile, the roll and yaw channels controlled by the ADRC also remain in a tighter range of reference commands than when controlled by the PID. As the ADRC provides a more stable flight, the tailsitter takes about 5s less than the time needed with the PID to complete the same maneuver. On the whole, the wind resistance in both tests demonstrates stability and excellent performance of the ADRC in disturbance rejection.

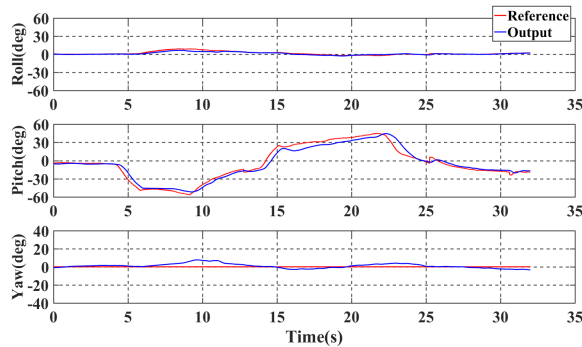


Fig. 11. Attitude of the tailsitter with ADRC in vertical flying

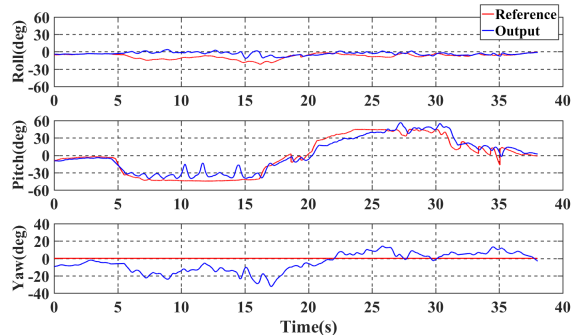


Fig. 12. Attitude of the tailsitter with PID in vertical flying

## VI. CONCLUSIONS AND FUTURE WORKS

The design and hovering control laws of the flying-wing tailsitter with two motors and two elevons are discussed in this paper. The vehicle configuration, including aircraft design and actuation principle, are presented first. Vehicle aerodynamics and a six-degrees-of-freedom model are developed for the tailsitter. The ADRC for attitude control and the cascade of P and PI controllers for position control are

proposed to achieve a better performance in outdoor stationary hovering and accurate vertical flying. Since both position and attitude controllers are independent of the vehicle model, they are available in engineering application. Experiments are presented to corroborate effectiveness of the controller in disturbance rejection. The on-going transition and horizontal flight of the tailsitter, as well as the ability to resist stronger winds, are the main future works.

## REFERENCES

- [1] K. Nonami, "Prospect and recent research & development for civil use autonomous unmanned aircraft as UAV and MAV," *Journal of system Design and Dynamics*, vol.1, no.2, pp.120-128, 2007.
- [2] R. Bapst, R. Ritz, L. Meier, and M. Pollefeys, "Design and implementation of an unmanned tailsitter," in *2015 IEEE/RSJ International Conference on Intelligent Robots and Systems (IROS)*, pp. 1885-1890, 2015.
- [3] A. Oosedo, S. Abiko, A. Konno, T. Koizumi, T. Furui and M. Uchiyama, "Development of a quad rotor tailsitter VTOL UAV without control surfaces and experimental verification," in *2013 IEEE International Conference on Robotics and Automation (ICRA)*, pp. 317-322, 2013.
- [4] S. Verling, B. Weibel, M. Boosfeld, K. Alexis, M. Burri, and R. Siegwart, "Full attitude control of a VTOL tailsitter UAV," in *2016 IEEE International Conference on Robotics and Automation (ICRA)*, pp. 3006-3012, 2016.
- [5] M. C. Kuang, J. H. Zhu, W. F. Wang, and Y. F. Tang, "Flight controller design and demonstration of a thrust-vectorred tailsitter," in *2017 IEEE International Conference on Robotics and Automation (ICRA)*, pp. 5169-5174, 2017.
- [6] N. B. Knoebel, and T. W. McLain, "Adaptive quaternion control of a miniature tailsitter UAV," in *2008 American Control Conference (ACC)*, pp. 2340-2345, 2008.
- [7] M. D. Hua, T. Hamel, P. Morin, and C. Samson, "A control approach for thrust-propelled underactuated vehicles and its application to VTOL drones," *IEEE Transactions on Automatic Control*, vol. 54, no. 8, pp. 1837-1853, 2009.
- [8] S. C. Kriel, "A comparison of control systems for the flight transition of vtol unmanned aerial vehicles," Ph.D. dissertation, University of Stellenbosch, 2008.
- [9] Y. Demitrit, S. Verling, T. Stastny, A. Melzer, and R. Siegwart, "Model-based wind estimation for a hovering VTOL tailsitter UAV," in *2017 IEEE International Conference on Robotics and Automation (ICRA)*, pp. 3945-3952, 2017.
- [10] T. Matsumoto, K. Kita, R. Suzuki, A. Oosedo, K. Go, Y. Hoshino, and M. Uchiyama, "A hovering control strategy for a tailsitter VTOL UAV that increases stability against large disturbance," in *2010 IEEE International Conference on Robotics and Automation (ICRA)*, pp. 54-59, 2010.
- [11] M. E. Argyle, R. W. Beard, and S. Morris, "The vertical bat tailsitter: dynamic model and control architecture," in *2013 American Control Conference (ACC)*, pp. 806-811, 2013.
- [12] L. Meier, D. Honegger, and M. Pollefeys, "PX4: A node-based multithreaded open source robotics framework for deeply embedded platforms," in *2015 IEEE International Conference on Robotics and Automation (ICRA)*, pp. 6235-6240, 2015.
- [13] W. Khan, and M. Nahon, "Development and Validation of a Propeller Slipstream Model for Unmanned Aerial Vehicles," *Journal of Aircraft*, vol. 52, no. 6, pp. 1985-1994, 2015.
- [14] T. Melin, "A vortex lattice MATLAB implementation for linear aerodynamic wing applications," Master dissertation, Royal Institute of Technology, 2000.
- [15] A. Deperrois, "XFLR5: a tool for the design of airfoils, wings and planes operating at low Reynolds numbers," Software Package, 2010.
- [16] Y. H. Wang, Y. Yao and K. M. Ma, "Error estimation of second order extended state observer," *Journal of Jilin University (Engineering and Technology Edition)*, vol. 40, no.1, pp. 143-147, 2010.
- [17] N. Kim, S. Cha, and H. Peng, "Optimal control of hybrid electric vehicles based on Pontryagin's minimum principle," *IEEE Transactions on Control Systems Technology*, vol. 19, no. 5, pp. 1279-1287, 2011.
- [18] W. Xue, and Y. Huang, "Comparison of the DOB based control, a special kind of PID control and ADRC," in *2011 American Control Conference (ACC)*, pp. 4373-4379, 2011.